NANO LETTERS

Letter

pubs.acs.org/NanoLett

Dual-Modal Magnetic Resonance and Fluorescence Imaging of Atherosclerotic Plaques in Vivo Using VCAM-1 Targeted Tobacco Mosaic Virus

Michael A. Bruckman,[†] Kai Jiang,[†] Emily J. Simpson,[⊥] Lauren N. Randolph,[†] Leonard G. Luyt,[⊥] Xin Yu,[†,‡] and Nicole F. Steinmetz*[,†,‡,§,∥]

[†]Department of Biomedical Engineering, [‡]Department of Radiology, [§]Department of Materials Science and Engineering, and [∥]Department of Macromolecular Engineering, Case Western Reserve University Schools of Medicine and Engineering, 10900 Euclid Avenue, Cleveland, Ohio 44106, United States

[⊥]Departments of Chemistry, Oncology, Medical Imaging, The University of Western Ontario, London, Ontario N6A 4L6, Canada

Supporting Information

ABSTRACT: The underlying cause of major cardiovascular events, such as myocardial infarctions and strokes, is atherosclerosis. For accurate diagnosis of this inflammatory disease, molecular imaging is required. Toward this goal, we sought to develop a nanoparticle-based, high aspect ratio, molecularly targeted magnetic resonance (MR) imaging contrast agent. Specifically, we engineered the plant viral nanoparticle platform tobacco mosaic virus (TMV) to target vascular cell adhesion molecule (VCAM)-1, which is highly expressed on activated endothelial cells at atherosclerotic plaques. To achieve dual optical and MR imaging in an atherosclerotic ApoE$^{-/-}$ mouse model, TMV was modified to carry near-infrared dyes and chelated Gd ions. Our results indicate molecular targeting of atherosclerotic plaques. On the basis of the multivalency and multifunctionality, the targeted TMV-based MR probe increased the detection limit significantly; the injected dose of Gd ions could be further reduced 400x compared to the suggested clinical use, demonstrating the utility of targeted nanoparticle cargo delivery.

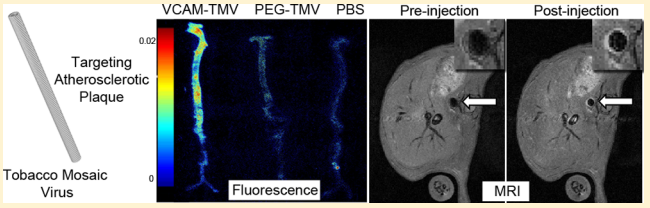

KEYWORDS: *Tobacco mosaic virus, magnetic resonance imaging, atherosclerosis, VCAM-1*

Heart disease is the leading cause of death in the U.S., and a large portion is attributed to atherosclerosis.[1] Atherosclerosis development can begin during adolescence and often remains asymptomatic until a clinical event such as a heart attack or stroke occurs. Early indicators of cardiovascular disease, such as unnatural levels of lipoproteins (including cholesterol), glucose, blood pressure, and body weight, are used to assess and prevent hospitalization and death resulting from a clinical event. However, all of these measurements are risk factors for atherosclerosis, not diagnosis of the disease. Current imaging methods to detect atherosclerosis include X-ray angiography,[2] optical coherence tomography,[3] and intravascular ultrasound[4] imaging; these are invasive methods that detect luminal narrowing and intima-media thickening. However, the risk of a clinical event depends more on the composition of the lesion as opposed to its size and luminal stenosis.[5] On the contrary, molecular imaging enables more accurate diagnosis of atherosclerotic plaques via sensitive detection of molecular biomarkers of vulnerable plaques. It also provides more comprehensive follow-up and assessment of pharmaceutical interventions.

Noninvasive imaging methods such as optical imaging, single-photon emission computed tomography, positron emission tomography, and magnetic resonance imaging (MRI) are currently in development and clinical testing.[6] Of these modalities, MR imaging is particularly attractive, because it is noninvasive, uses nonionizing radiation, while facilitating deep tissue imaging and providing high soft tissue contrast. While MR imaging provides high spatial resolution, diagnosis can be difficult in areas where diseased and healthy tissues are of similar signal intensities. This lack of imaging contrast can be overcome by using contrast-enhancement agents and nanoparticle formulations that target highly expressed molecular epitomes in the diseased tissue.

Atherosclerosis is characterized by the accumulation of lipids (carrying cholesterol), leukocytes, fibrous elements, and smooth muscle cells into the intima of arteries. A key process during atherosclerotic plaque development is the infiltration of leukocytes:[7] activated endothelial cells that express proinflammatory molecules including E- and P-selectins, vascular cell adhesion molecule-1 (VCAM-1), and intercellular adhesion molecule-1, which support rolling, adhesion, and migration of leukocytes.[8] In addition, the following molecular and cellular targets are present in plaque development and have been used

Received: December 29, 2013
Revised: February 2, 2014
Published: February 6, 2014

   dx.doi.org/10.1021/nl404816m | *Nano Lett.* 2014, 14, 1551−1558

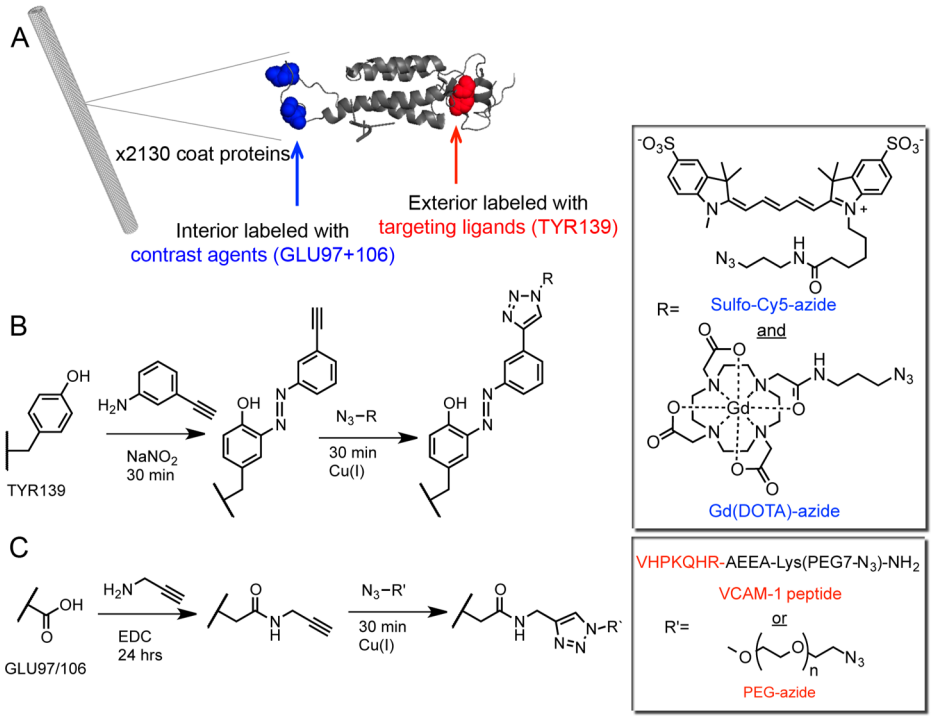

Figure 1. (A) An illustrative image (PyMol and Chimera) of the structure of tobacco mosaic virus rods and its coat protein. The exterior (red) and interior (blue) reactive amino acids are highlighted in the individual coat protein. Bioconjugation of VCAM-1 targeting ligands or PEG and contrast agents to the surface of TMV involved the following sequence of reactions: (B) exterior incorporation of alkynes followed by attachment of VCAM-1 or PEG, followed by (C) internal channel incorporation of alkynes and contrast agent modification. Chemical structures are shown in the boxes.

to identify and classify plaque development: fibrin, scavenger receptors, annexin V, and $\alpha_v\beta_3$ integrin.[9] These molecular signatures of the inflamed endothelium open the door for targeted, molecular imaging tools.

VCAM-1 is an attractive target because of its critical role in atherosclerosis development and its unique expression pattern: VCAM-1 is highly up-regulated on inflamed endothelium.[10] Indeed, several molecular imaging applications of nanoparticle formulation targeted to VCAM-1 have been demonstrated, such as perfluorocarbons,[11,12] iron oxides,[13,14] polymers,[15] and quantum dots.[16]

To date, the nanoparticle systems tested and developed for molecular imaging of atherosclerosis are of spherical nature, which may not be optimal. There is emerging evidence suggesting that nonspherical materials have superior properties, especially for endothelial targeting; increased margination toward the vessel wall increases the probability for the imaging probe to effectively interact with the molecular target. Furthermore, the elongated materials present the ligands more effectively to the much larger and flat vessel wall compared to spherical nanoparticles (with their high degree of curvature).[17−19] Another advantage is that elongated materials have increased immune evasion and reduced macrophage uptake, therefore further contributing to synergistic target enhancement as a combination of molecular recognition and particle morphology.[20,21]

While a few studies have investigated the application of nonspherical materials for applications in cancer nanotechnology and medicine,[22,23] the study of elongated materials for applications in cardiovascular disease remains an understudied area. It remains challenging to precisely control the synthesis of nanoparticles in two dimensions, and therefore most materials under development spherical symmetry. We have turned toward high aspect ratio (defined as length over width) nanomaterials produced by nature, specifically, the tubular structures forming the plant virus tobacco mosaic virus (TMV) measuring 300 × 18 nm. TMV and other plant viral nanoparticles (VNPs) have many beneficial properties for medical applications. Its structure is known to atomic resolution and its surface chemistry (inside and out) is well-established;[24] in addition, TMV is amenable to genetic engineering at its solvent-exposed *N*- and *C*-terminus.[25−28] Structure-based engineering allows the introduction of deterministic, precise, and reproducible modifications. The production of TMV using molecular farming in plants is highly scalable and economic (and does not involve toxic solvents or high-temperature processes). We have shown that TMV can be delivered intravenously and is biocompatible and biodegradable.[29] Short circulation times (minutes) and rapid tissue clearance make it an ideal candidate for applications in molecular imaging. In this study, we report the application of TMV as a platform for dual molecular optical and MR imaging of atherosclerotic plaques using the ApoE$^{-/-}$ mouse model.

TMV was propagated and isolated from *Nicotiana benthamiana* plants. Figure 1A shows the high-resolution crystal structure of TMV highlighting exterior tyrosine residues (TYR139, red) and interior glutamic acid residues (GLU97/106, blue) that were functionalized using previously established protocols.[30] TMV was labeled with sulfo-Cy5-azide dyes for optical imaging, Gd ions chelated with azido-mono amide-1,4,7,10-tetraazacyclododecane-*N*-*N*′-*N*″-*N*‴-tetra acetic acid (Gd(DOTA)) for MR imaging, PEG, and oligopeptides (VHPKQHRAEEA-Lys(PEG7-N_3)-NH_2),[31] specific to VCAM-1 receptor (Figure 1B). Detailed experimental procedures as well as peptide synthesis and characterization are described in the Supporting Information. In brief, a

dx.doi.org/10.1021/nl404816m | *Nano Lett.* 2014, 14, 1551−1558

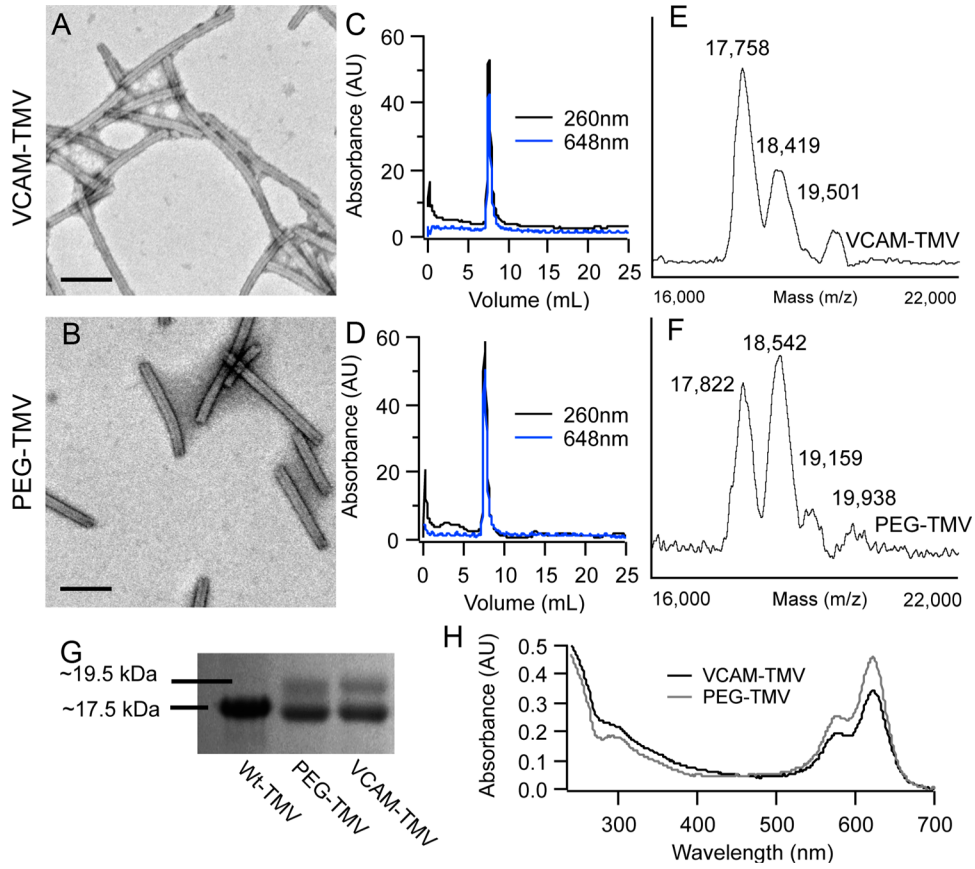

Figure 2. Bioconjugation of TMV was characterized by TEM, SEC, MALDI-TOF MS, SDS-PAGE, and UV−vis absorbance. The TEM of (A) VCAM-TMV and (B) PEG-TMV show that the rod shape of TMV is maintained after modification (scale bar is 100 nm). The single and aligned peaks from SEC absorbance at 260 and 647 nm of (C) VCAM-TMV and (D) PEG-TMV indicate that the particles are pure, monodisperse, and that the Cy5 dyes are covalently attached to TMV. (E) MALDI-TOF MS of VCAM-TMV displays peaks associated with either wt-TMV or alkyne-TMV CPs (17 758 m/z), CPs labeled with a single contrast agent (Gd(DOTA) or Cy5) (18 419 m/z), and CPs labeled with a VCAM peptide (19 501 m/z). Similarly, (F) the MS of PEG-TMV displays peaks associated with either wt-TMV or alkyne-TMV CPs (17 822 m/z), CPs labeled with a single contrast agent (18 542 m/z) or two contrast agents (19 159 m/z), and CPs labeled with a PEG molecule (19 938 m/z). More detailed analysis of MALDI-TOF MS is provided in the Supporting Information. (G) SDS-PAGE after Coomassie staining of 1 = unmodified TMV, 2 = VCAM-TMV, 3 = PEG-TMV. (H) UV−vis absorbance of VCAM-TMV (black line) and PEG-TMV (gray line).

combination of carbodiimide coupling targeting interior glutamic acids and diazonium coupling targeting exterior tyrosine side chains was used to introduce alkyne ligation handles, followed by introduction of functional molecules (contrast agents and peptide ligand) using copper-catalyzed azide-alkyne cycloaddition (CuAAC) chemistry (Figure 1B,C, Supporting Information). The sequence of chemical reactions was critical to ensure particle stability. First the exterior surface is modified with alkyne handles followed by modification with PEG or VCAM-1 peptide (Figure 1B); second, the interior is modified with alkyne handles followed by modification with optical and MR contrast agents (Figure 1C).

Transmission electron microscopy (TEM) and size exclusion chromatography (SEC) analysis indicate that the modified TMV particles remained structurally sound following multiple rounds of bioconjugation reactions (TEM of VCAM-TMV and PEG-TMV shown in Figure 2A,B, respectively). SEC also indicates covalent modification of TMV with Cy5 dyes as indicated by coelution of the dye-specific peak at 648 nm with the TMV peak at 260 nm (Figure 2C,D). A combination of denaturing gel electrophoresis (SDS-PAGE), matrix-assisted laser desorption-ionization time-of-flight mass spectrometry (MALDI-TOF MS), UV−visible spectroscopy, and inductively coupled plasma optical emission spectroscopy (ICP-OES) measurements were performed to determine the degree of labeling (Figure 2). Figure 2E shows the MALDI-TOF MS for VCAM-TMV coat proteins (CPs) displaying peaks attributed to a mix of (i) alkyne-modified CPs (17 758 m/z), (ii) contrast agent (Gd(DOTA) or Cy5)-modified CPs (18 419 m/z), and (iii) VCAM peptide-modified CPs (19 501 m/z). Similarly, Figure 2F shows the MS of PEG-TMV with peaks attributed to a mix of (i) alkyne-modified CP (17 822 m/z), (ii) CPs with one contrast agent-modified CP (18 542 m/z) or CPs with two contrast agents per CP (19 159 m/z), and (iii) PEG-modified CPs (19 938 m/z). While dual modification of the CPs with targeting ligand and contrast agents was not observed, data indicate collective labeling of the TMV rod consisting of a mix of CPs labeled with either a Cy5 NIR dye, Gd(DOTA) MR contrast agent, and the VCAM-1 targeting ligand or PEG. Detailed mass spectra, theoretical mass of TMV CP products after each conjugation step, and their peak assignments are provided in the Supporting Information; see Supporting Information Figures S1 and S2 and Tables S1 and S2. It should be noted that MALDI-TOF MS is not a quantitative method but can confirm qualitatively covalent modifications.[32]

dx.doi.org/10.1021/nl404816m | Nano Lett. 2014, 14, 1551−1558

Quantitative labeling of TMV coat proteins was confirmed with SDS-PAGE of the TMV coat proteins with VCAM-1 ligand and PEG (as indicated by the higher molecular weight bands); band lane analysis using ImageJ software (Figure 2G) indicates coverage of TMV with ~500 VCAM-1 ligands and PEG molecules, respectively, which corresponds to 25% of the coat proteins being modified (TMV consists of 2130 identical coat proteins). UV−visible absorbance was used to determine the degree of Cy5 labeling and ICP-OES was used to determine the number of Gd(DOTA) molecules per TMV rod. We found that VCAM-TMV and PEG-TMV were labeled with ~460 and ~510 Cy5 dyes, respectively, thus also covering 25% of the available coat proteins. Finally, VCAM-TMV was loaded with ~1200 chelated Gd ions, resulting in a per Gd relaxivity of 14.6 mM^{-1} s^{-1} yielding a per TMV relaxivity of 17, 567 mM^{-1} s^{-1} at 60 MHz (Figure 2). This is a 3-fold increase in ionic relaxivity over free Gd(DOTA) (5 mM^{-1} s^{-1} at 60 MHz) resulting from the reduced molecular tumbling rate.[33]

TMV sensors were tested *in vivo* using the well-established $ApoE^{-/-}$ mouse model, fed on a high fat/cholesterol diet for 14−18 weeks.[34] All procedures were carried out according to IACUC approved protocols. Mice were injected with 10 mg/kg VCAM-TMV (n = 4) and PEG-TMV (n = 3), respectively. Control animals were injected with PBS and concentration matched nontargeted contrast agent (sulfo-Cy5-azide in PBS). The injected dose of Cy5 used was 0.20 mg/kg (2.5×10^{-4} mmol/kg); matched to the concentration of Cy5 injected in 10 mg/kg VCAM-TMV. Finally, VCAM-TMV was injected into age-matched healthy mice C57BL/6 to demonstrate that VCAM-TMV particles did not accumulate at healthy endothelial cells. TMV-based imaging sensors and respective controls were administered intravenously into the tail vein and the samples were allowed to circulate for up to 3 h prior to dissection and *ex vivo* fluorescence analysis of the aortas using Maestro imaging system (Figure 3). Fluorescence imaging indicates selective targeting and accumulation of VCAM-TMV in the diseased aortas; quantitative image analysis using Maestro imaging software indicates 3-fold increased accumulation of VCAM-TMV versus PEG-TMV and therefore demonstrates molecular targeting (see also discussion below).

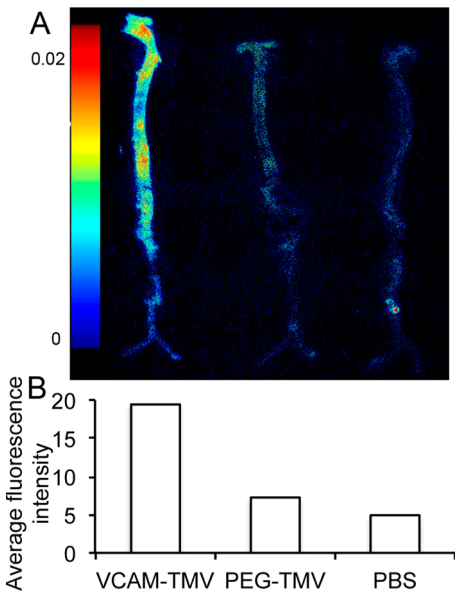

Figure 3. (A) *Ex vivo* fluorescence of aortas from $ApoE^{-/-}$ mice injected with (from left to right) VCAM-TMV, PEG-TMV, PBS. (B) Quantitative image analysis (bar graph) showing average fluorescence intensity per sample.

Localization of targeted VCAM-TMV in atherosclerotic plaques was further confirmed by immunofluorescence imaging of cryosectioned aortas. Sections of aortas were stained for macrophages (CD68 antibody) to confirm the presence of plaques (detailed procedures are listed in the Supporting Information). Representative images of sectioned and stained aortas from mice injected with VCAM-TMV and PEG-TMV, and PBS are shown in Figure 4. In addition, we imaged sectioned aortas from $ApoE^{-/-}$ mice injected with free sulfo-Cy5 dye as well as aortas from healthy C57Bl/6 mice injected with VCAM-TMV; analysis of these aortas indicated no fluorescent signal (sectioned images not shown).

We qualitatively analyzed aortas from each mouse for plaque coverage and TMV accumulation. Aortas were cut into 10−12 sections 2−4 mm long sections and embedded into OCT medium. The sections were then categorized as being positive or negative for plaque based on morphology and positive macrophage staining. Then, sections were further categorized as positive or negative for fluorescence (Cy5) signal. While VCAM-TMV accumulation was confirmed in 70% of plaque sections, only 18% of plaque sections were positive for PEG-TMV signal, indicating VCAM-specific targeting of the VCAM-TMV formulation. VCAM-TMV and PEG-TMV was not detected in healthy aorta sections and any other negative controls. Overall, our data support molecular targeting of VCAM-TMV to inflamed endothelium.

Imaging indicated that VCAM-TMV was localized at the intima-media surface of the plaque, the location of activated endothelial cells expressing VCAM-1 receptors.[10] There was no indication that VCAM-TMV particles were taken up by macrophages and incorporated into plaques. The distribution of PEG-TMV and VCAM-TMV within the plaque tissue was similar, however, a significantly higher uptake was observed using the targeted VCAM-TMV formulation.

MR imaging of $ApoE^{-/-}$ mice was conducted on a Bruker BioSpin 7.0T 70/30USR MRI system. Gd(DOTA)-labeled VCAM-TMV was injected via a tail vein catheter. Several negative controls were used such as free Gd(DOTA) and PBS injected into $ApoE^{-/-}$ mice as well as VCAM-TMV injected into healthy C57Bl/6 mice. The injected dose of Gd was 0.20 mg/kg (2.5×10^{-4} mmol/kg), which is 400 times lower than typical MRI contrast agent of 0.1 mmol/kg for Gadovist, which is the closest chemically related clinical contrast agent to Gd(DOTA). The Gd concentration was chosen based on the amount of Gd injected with 10 mg/kg VCAM-TMV. Following multiple scouting scans, T_1-weighted images were acquired at baseline and at 30, 60, and 90 min postinjection. A total of 8-axial slices were acquired with 1 mm slice thickness and 1.5 mm slice separation. Image acquisition used a fat-suppressed, respiration and ECG-triggered, multislice multiecho (MSME) black-blood sequence optimized to delineate the aortic wall with the following parameters: TR/TE = 600/8.0 ms, two averages, matrix size = 256 × 256, and field of view = 2.98 × 2.98 cm^2. Scan time including triggering was 15−20 min. Signal to noise ratio (SNR) was calculated by dividing the average intensity of the aortic vessel wall by the standard deviation of an area outside the mouse body.

A mouse injected with VCAM-TMV saw an increase in SNR from 12.6 (preinjection) to 14.7 (20 min), 21.5 (60 min), and 28.7 (95 min) (Figure 5A). The increase in SNR increased over

dx.doi.org/10.1021/nl404816m | *Nano Lett.* 2014, 14, 1551−1558

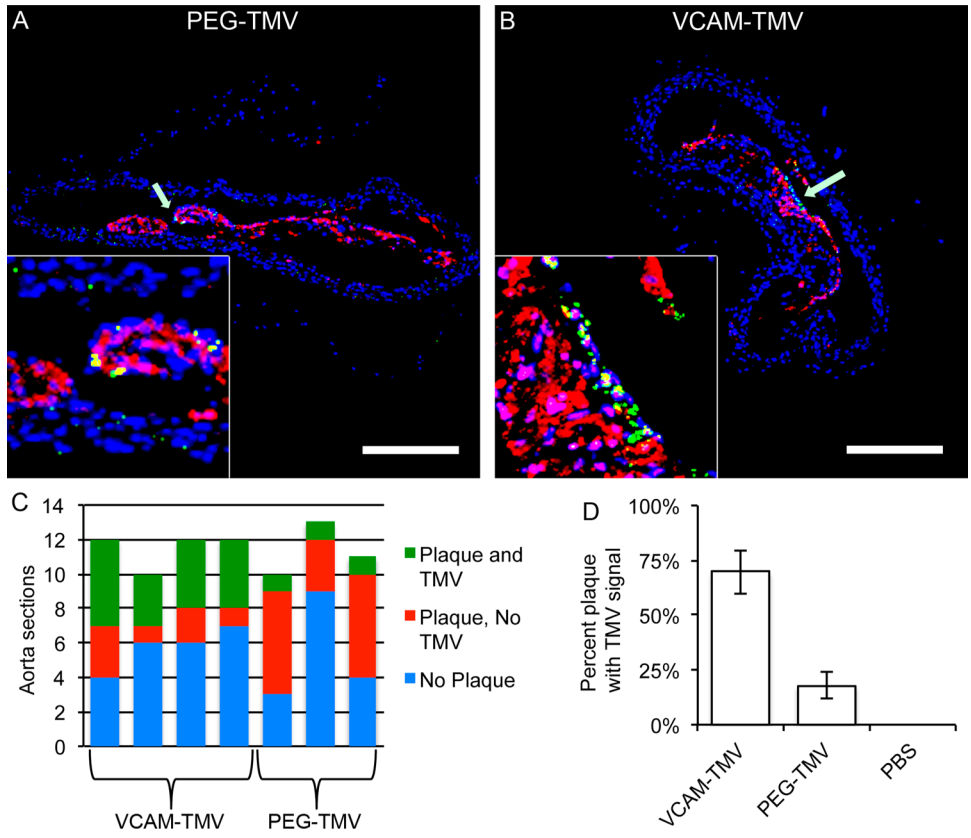

Figure 4. Representative confocal images of cryosectioned aortas from ApoE$^{-/-}$ mice injected with (A) PEG-TMV, and (B) VCAM-TMV (imaging was performed based on the sulfo-Cy5 label, particles are pseudocolored in green. Macrophages (CD68 stain) are shown in red and nuclei (stained with DAPI) are shown in blue. Scale bar = 250 μm. The inset represents a magnified view of the plaque intima (see arrow). (C) The aorta from each mouse was cut into 10−12 sections 2−4 mm long and then analyzed for plaque content. Results are plotted as a bar graph quantifying the number of sections without plaque (blue), sections containing plaque but no signal from TMV (red), and sections containing plaque with signal from TMV (green). (D) This data is summarized as percentage of aorta sections with plaque and TMV signal. Seventy percent of the aorta sections from ApoE$^{-/-}$ mice injected with VCAM-TMV contained TMV fluorescence, whereas only 18% for PEG-TMV.

time and peaked around 90 min. Not all slices indicated increase in SNR. This is consistent with histological analysis of collected aortas that indicated that about 50% of the aortas contained plaques, and that 70% of those plaques contained TMV. The SNR for free Gd(DOTA) (0.2 mg/kg) and PBS injected into ApoE$^{-/-}$ mice and VCAM-TMV injected (10 mg/kg) into a healthy C57Bl/6 mouse remained between 10 and 15 (Figure 5B−D, respectively). In summary, our data support that VCAM-TMV delivers large payloads of Gd(DOTA) enabling sensitive detection and imaging of atherosclerotic plaques in mice. Non-specific accumulation of non-targeted TMV sensors of false positive signals in healthy mice aortas was not observed.

For the first time, we report the application of a plant virus-based T_1 contrast agent for medical MR imaging. TMV-based nanorods were loaded with contrast agents and fluorophores for dual MR and optical imaging; further, TMV was modified with peptides targeting VCAM-1 receptors, which are highly expressed in developing atherosclerotic plaques. A combination of *ex vivo* optical imaging and immunofluorescence microscopy supports molecular targeting and imaging of VCAM-1 signatures in a mouse model of atherosclerosis. Nontargeted PEG-TMV (negative control) formulations showed negligible passive accumulation in the diseased aortas. Immunofluorescence imaging was consistent with VCAM-TMV accumulation at the intima-media interface of the plaque, which is in agreement with the expression pattern of VCAM-1 receptors.[10]

The development of *in vivo* diagnostics and screening methods for detection of atherosclerotic plaques at risk of rupturing is an important goal in medicine and holds the potential to reduce the numbers of heart attacks and strokes. Clinical approaches utilize coronary angiography,[2] optical coherence tomography,[3] and intravascular ultrasound.[4] Drawbacks are that these methods involve invasive procedures and rely on stenosis (lumen narrowing and vessel wall thickening); however, data indicate that stenosis correlates poorly with the risk of plaque rupture. It has been recognized that the accurate diagnosis of plaques vulnerable to rupturing requires non-invasive identification of specific molecular markers, which is currently an unmet clinical need.[35]

In recent years, significant advances have been made toward translating the biology of atherosclerosis to highlight markers for molecular targeting.[8] For example, the general characteristics of vulnerable plaques include high macrophage content, thin fibrin cap, and intimal remodeling. The expression pattern of VCAM-1 receptors on endothelial cells is relatively well understood: its function is to recruit leukocytes to the arterial intima; therefore VCAM-1 expression is a strong indicator of continued plaque development. Indeed, several groups demonstrated molecular imaging of VCAM-1 receptors using either small peptides or antibodies appended to perfluor-

dx.doi.org/10.1021/nl404816m | *Nano Lett.* 2014, 14, 1551−1558

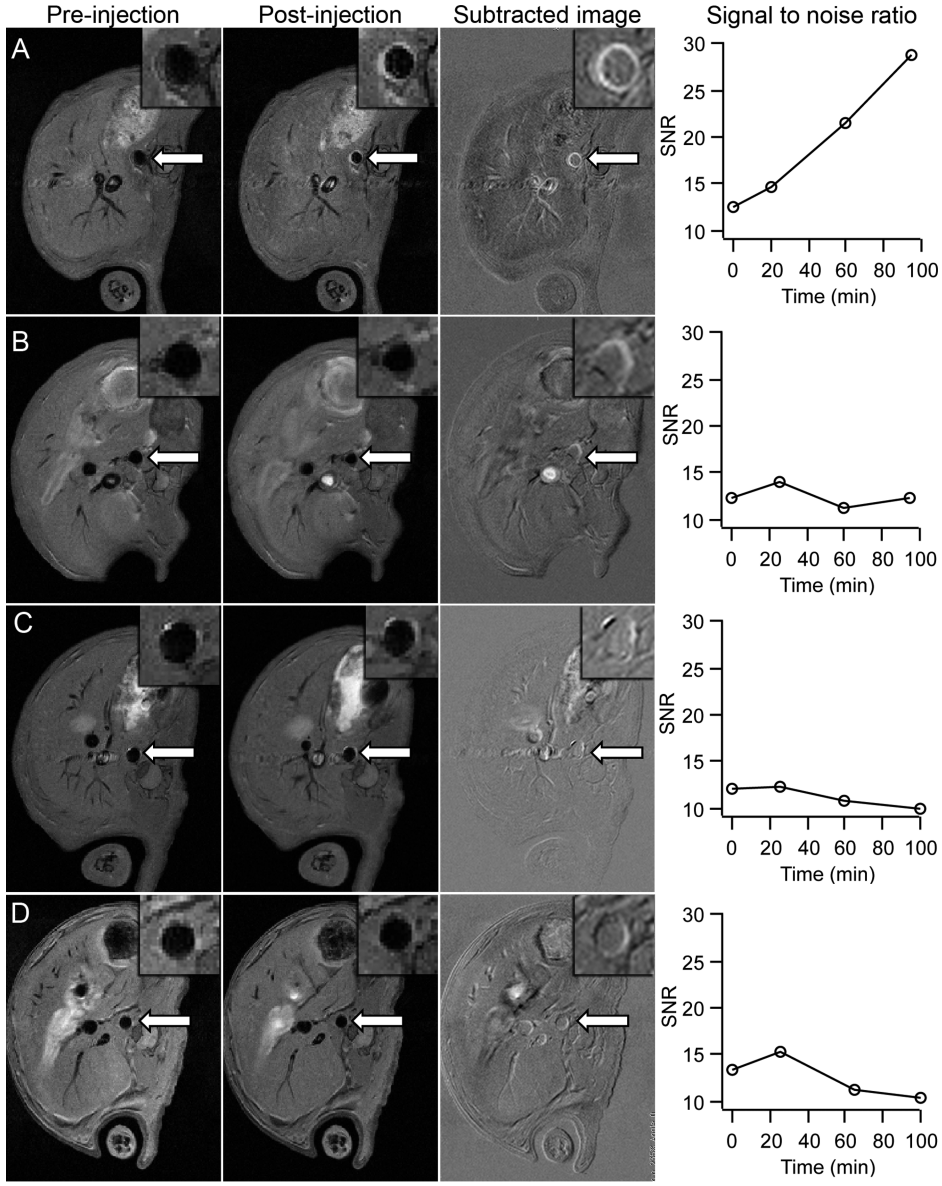

Figure 5. Pre- and postinjection MRI scans of (A) VCAM-TMV, (B) Gd(DOTA), and (C) PBS in ApoE$^{-/-}$ mice, and (D) VCAM-TMV in a C57Bl/6 mouse. The third column is the subtracted image (90 min postinjection minus preinjection). The fourth column is the signal-to-noise ratio (SNR) for the vessel wall of the aortas. Insets are magnified images of the abdominal aorta regions of interest.

ocarbons,[11,12] as free peptides/antibody,[12,36] and metallic nanoparticles.[37] Other approaches include targeting molecular signatures such as fibrin,[38,39] elastin,[40] vimentin,[41] and apoptotic cells.[42] Synthetic and nature's nanoparticles have been developed as targeted devices for imaging of the inflamed endothelium. For example, others have shown targeting of 30 nm sized icosahedron cowpea mosaic virus (CPMV) to atherosclerotic plaques,[41,43] based on its naturally occurring interactions with surface-expressed vimentin receptors present on macrophages and foam cells. In a different approach, a small heat shock protein genetically encoded with the oligopeptide LyP-1 was used to target atherosclerosis-associated macrophages.[44] However, *in vivo* imaging modalities, such as MRI, have not been demonstrated using CPMV or other protein-based nanoparticles.

Nanoparticle-based T_1 contrast agents loaded with high payloads of chelated Gd have been developed and studied for MR imaging. The advantages of using nanocarriers is the increased SNR resulting from combined contribution of large payload delivery, molecular targeting, and reduced tumbling rates. Nevertheless, the concern is that nanoparticles loaded with gadolinium ions may lead to increased toxicity due to enhanced tissue retention and potential release of free Gd ions.[45] Free Gd ions are susceptible to transmetallization causing inflammatory responses in nearly all tissues.[46,47] Chelating Gd ions to molecules such as DOTA significantly reduces this effect but not completely. Injecting chelated Gd into patients with kidney disease has led to nephrogenic systemic fibrosis due to the kidneys inability to clear the paramagnetic contrast agent quickly.[48,49] Using TMV-based contrast agents may offer a possible solution to this translational hurdle: TMV-based contrast agents have a short circulation time with a plasma half-life on the order of minutes. The combination of rapid blood pool clearance and rapid accumulation at the target side (maximum SNR was reached in MRI 90 min post VCAM-TMV administration) provides a

dx.doi.org/10.1021/nl404816m | *Nano Lett.* 2014, 14, 1551−1558

suitable time frame for imaging applications; for example, it would be ideal to inject the patient on the way to the MRI (rather than hours prior to imaging). In a recent study documenting the biodistribution, pharmacokinetics, and blood compatibility, we demonstrated that TMV shows good biocompatibility and is cleared from tissues within hours to days post administration with no apparent pathological side effects.[29]

Most importantly, we would like to stress that the TMV-based contrast agent allowed molecular MR imaging at an injected dose 400 times lower than the clinical dose of chelated Gd molecules used in exams such as magnetic resonance angiography; we report imaging of atherosclerotic plaques at a dose of 0.00025 mmol/kg Gd ions versus 0.1 mmol/kg Gd ions (typical clinical dose). For comparison, recently published paramagnetic nanoparticle platforms generally use injected doses of 0.01 to 0.05 mmol/kg Gd.[39,42,50,51] The significant increase in sensitivity can be explained by the large payload of Gd ions delivered per particle in combination with molecular targeting and reduced tumbling rates (effect of shape) increasing the relaxivity per ion. To the best of our knowledge, this is the lowest injection dose of chelated Gd yielding adequate positive signal enhancement in a preclinical atherosclerotic mouse model.

Here, we hypothesize that the elongated shape of TMV contributes synergistically to the molecular targeting strategy. Recent reports indicate that elongated, rod-shaped nanoparticles have improved margination properties and therefore enhanced vessel wall targeting compared to spherical particles; furthermore, increased circulation and decreased phagocytosis, as well as increased surface area along with higher density of targeting ligands, are factors that contribute to favorable *in vivo* properties based on shape effects.[52]

While molecular imaging holds the potential to enable screening and early detection of atherosclerotic plaques, molecular targeting strategies could be combined with therapeutic approaches (leading toward the development of theranostics). Expression of VCAM-1 receptors on endothelial cells is present throughout all stages of the plaque development.[9] VCAM-1 expression decreases in patients upon treatment with statins or angiotensin antagonists, further supporting its critical role in atherosclerotic development.[53,54] Interestingly, blocking VCAM-1 receptors has a demonstrated therapeutic effect by interfering with the inflammatory signaling cascade that results from lipid accumulation.[55] Also, the lack of leukocyte recruitment (inherent with reduced VCAM-1 expression) is expected to lead to reduced macrophage and foam cell presence, therefore reducing the risk of plaque rupture.

In summary, our data support the successful development of a molecularly targeted TMV-based probe for dual MR and optical imaging of atherosclerotic plaques in mice. We demonstrated that large payloads of cargo (here contrast agents) were delivered to atherosclerotic plaques by targeting molecular cell receptors present on activated endothelial cells. While this study focuses on the application of TMV-based sensors for MR detection and imaging of atherosclerotic plaques, the developed imaging probes could also find application for MR imaging of other diseases. Furthermore, the contrast agents could be exchanged with therapeutic agents and/or therapeutic moieties could further be added to the multifunctional scaffold. It is clear that the molecular structure of TMV offers a high degree of engineerability (TMV particles remained stable after multiple rounds of bioconjugation). The potential applications of the TMV-based plug'n play technology are wide-ranging and future studies will include imaging of combinations of molecular targets as well as drug delivery.

■ ASSOCIATED CONTENT

Ⓢ Supporting Information

Experimental protocols and supporting data are supplied. This material is available free of charge via the Internet at http://pubs.acs.org.

■ AUTHOR INFORMATION

Corresponding Author

*E-mail: nicole.steinmetz@case.edu. Telephone: 216-844-8164.

Author Contributions

All authors contributed to the experimental data and writing of the manuscript. All authors have given approval to the final version of the manuscript.

Notes

The authors declare no competing financial interest.

■ ACKNOWLEDGMENTS

This work was supported by Mt. Sinai Foundation, NIH training Grant T32 HL105338 and the Natural Sciences and Engineering Research Council of Canada. The authors also acknowledge the National Science Foundation Science and Technology Center for Layered Polymeric Systems (CLiPS) for the confocal microscopy user facility (DMR-0423914).

■ ABBREVIATIONS

TMV, tobacco mosaic virus; MRI, magnetic resonance imaging; SNR, signal-to-noise; VNP, viral nanoparticle; VCAM, vascular cell adhesion molecule; PEG, polyethylene glycol; TEM, transmission electron microscopy; SEC, size exclusion chromatography; MALDI-TOF MS, matrix-assisted laser desorption-ionization time-of-flight mass spectrometry; SDS-PAGE, sodium dodecyl sulfate polyacrylamide gel electrophoresis; UV−vis, ultraviolet−visible; ICP-OES, inductively coupled plasma-optical emission spectroscopy; ECG, electrocardiogram; TR, repetition time; TE, echo time; CPMV, cowpea mosaic virus

■ REFERENCES

(1) Lloyd-Jones, D.; Adams, R. J.; Brown, T. M.; Carnethon, M.; Dai, S.; De Simone, G.; Ferguson, T. B.; Ford, E.; Furie, K.; Gillespie, C.; Go, A.; Greenlund, K.; Haase, N.; Hailpern, S.; Ho, P. M.; Howard, V.; Kissela, B.; Kittner, S.; Lackland, D.; Lisabeth, L.; Marelli, A.; McDermott, M. M.; Meigs, J.; Mozaffarian, D.; Mussolino, M.; Nichol, G.; Roger, V. L.; Rosamond, W.; Sacco, R.; Sorlie, P.; Stafford, R.; Thom, T.; Wasserthiel-Smoller, S.; Wong, N. D.; Wylie-Rosett, J. *Circulation* **2010**, *121* (7), e46−e215.

(2) Puri, R.; Tuzcu, E. M.; Nissen, S. E.; Nicholls, S. J. *Int. J. Cardiol.* **2013**, *168* (2), 670−679.

(3) Rieber, J.; Meissner, O.; Babaryka, G.; Reim, S.; Oswald, M.; Koenig, A.; Schiele, T. M.; Shapiro, M.; Theisen, K.; Reiser, M. F.; Klauss, V.; Hoffmann, U. *Coron. Artery Dis.* **2006**, *17* (5), 425−430.

(4) Hartmann, M.; Huisman, J.; Bose, D.; Jensen, L. O.; Schoenhagen, P.; Mintz, G. S.; Erbel, R.; von Birgelen, C. *Eur. J. Echocardiogram* **2011**, *12* (4), 313−321.

(5) Virmani, R.; Burke, A. P.; Farb, A.; Kolodgie, F. D. *J. Am. Coll. Cardiol.* **2006**, *47* (8 Suppl), C13−C18.

(6) Gallino, A.; Stuber, M.; Crea, F.; Falk, E.; Corti, R.; Lekakis, J.; Schwitter, J.; Camici, P.; Gaemperli, O.; Di Valentino, M.; Prior, J.; Garcia-Garcia, H. M.; Vlachopoulos, C.; Cosentino, F.; Windecker, S.;

Pedrazzini, G.; Conti, R.; Mach, F.; De Caterina, R.; Libby, P. *Atherosclerosis* **2012**, *224* (1), 25−36.
(7) Swirski, F. K.; Nahrendorf, M. *Science* **2013**, *339* (6116), 161−166.
(8) Libby, P.; Ridker, P. M.; Hansson, G. K. *Nature* **2011**, *473* (7347), 317−325.
(9) Quillard, T.; Libby, P. *Circ. Res.* **2012**, *111* (2), 231−244.
(10) Iiyama, K.; Hajra, L.; Iiyama, M.; Li, H.; DiChiara, M.; Medoff, B. D.; Cybulsky, M. I. *Circ. Res.* **1999**, *85* (2), 199−207.
(11) Pan, H.; Myerson, J. W.; Hu, L.; Marsh, J. N.; Hou, K.; Scott, M. J.; Allen, J. S.; Hu, G.; San Roman, S.; Lanza, G. M.; Schreiber, R. D.; Schlesinger, P. H.; Wickline, S. A. *FASEB J.* **2013**, *27* (1), 255−264.
(12) Southworth, R.; Kaneda, M.; Chen, J.; Zhang, L.; Zhang, H.; Yang, X.; Razavi, R.; Lanza, G.; Wickline, S. A. *Nanomedicine* **2009**, *5* (3), 359−367.
(13) Michalska, M. M.; Machtoub, L. L.; Manthey, H. D. H.; Bauer, E. E.; Herold, V. V.; Krohne, G. G.; Lykowsky, G. G.; Hildenbrand, M. M.; Kampf, T. T.; Jakob, P. P.; Zernecke, A. A.; Bauer, W. R. W. *Arterioscler. Thromb. Vasc. Biol.* **2012**, *32* (10), 2350−2357.
(14) Burtea, C.; Ballet, S.; Laurent, S.; Rousseaux, O.; Dencausse, A.; Gonzalez, W.; Port, M.; Corot, C.; Elst, L. V.; Muller, R. N. *Arterioscler. Thromb. Vasc. Biol.* **2012**, *32* (6), e36−e48.
(15) Deosarkar, S. P.; Malgor, R.; Fu, J.; Kohn, L. D.; Hanes, J.; Goetz, D. J. *Biotechnol. Bioeng.* **2008**, *101* (2), 400−407.
(16) Jayagopal, A.; Russ, P. K.; Haselton, F. R. *Bioconjugate Chem.* **2007**, *18* (5), 1424−1433.
(17) Doshi, N.; Prabhakarpandian, B.; Rea-Ramsey, A.; Pant, K.; Sundaram, S.; Mitragotri, S. *J. Controlled Release* **2010**, *146* (2), 196−200.
(18) Lee, S. Y.; Ferrari, M.; Decuzzi, P. *Nanotechnology* **2009**, *20* (49), 495101.
(19) Tan, J.; Shah, S.; Thomas, A.; Ou-Yang, H. D.; Liu, Y. *Microfluid. Nanofluid.* **2013**, *14* (1−2), 77−87.
(20) Vácha, R.; Martinez-Veracoechea, F. J.; Frenkel, D. *Nano Lett.* **2011**, *11* (12), 5391−5395.
(21) Arnida; Janat-Amsbury, M. M.; Ray, A.; Peterson, C. M.; Ghandehari, H. *Eur. J. Pharm. Biopharm.* **2011**, *77* (3), 417−423.
(22) Shukla, S.; Wen, A. M.; Ayat, N. R.; Commandeur, U.; Gopalkrishnan, R.; Broome, A. M.; Lozada, K. W.; Keri, R. A.; Steinmetz, N. F. *Nanomedicine* **2013**.
(23) Smith, B. R.; Kempen, P.; Bouley, D.; Xu, A.; Liu, Z.; Melosh, N.; Dai, H.; Sinclair, R.; Gambhir, S. S. *Nano Lett.* **2012**, *12* (7), 3369−3377.
(24) Bruckman, M. A.; Hern, S.; Jiang, K.; Flask, C. A.; Yu, X.; Steinmetz, N. F. *J. Mater. Chem. B* **2013**, *1* (10), 1482−1490.
(25) Fitchen, J.; Beachy, R. N.; Hein, M. B. *Vaccine* **1995**, *13* (12), 1051−1057.
(26) Fujiyama, K.; Saejung, W.; Yanagihara, I.; Nakado, J.; Misaki, R.; Honda, T.; Watanabe, Y.; Seki, T. *J. Biosci. Bioeng.* **2006**, *101* (5), 398−402.
(27) Koo, M.; Bendahmane, M.; Lettieri, G. A.; Paoletti, A. D.; Lane, T. E.; Fitchen, J. H.; Buchmeier, M. J.; Beachy, R. N. *Proc. Natl. Acad. Sci. U.S.A.* **1999**, *96* (14), 7774−7779.
(28) Smith, M. L.; Fitzmaurice, W. P.; Turpen, T. H.; Palmer, K. E. *Curr. Top. Microbiol. Immunol.* **2009**, *332*, 13−31.
(29) Bruckman, M. A.; Randolph, L. N.; VanMeter, A.; Hern, S.; Shoffstall, A. J.; Steinmetz, N. F. *Virology* **2014**, *449*, 163−173.
(30) Bruckman, M. A.; Hern, S.; Jiang, K.; Flask, C. A.; Yu, X.; Steinmetz, N. F. *J. Mater. Chem. B* **2013**, *1* (10), 1482−1490.
(31) Nahrendorf, M.; Jaffer, F. A.; Kelly, K. A.; Sosnovik, D. E.; Aikawa, E.; Libby, P.; Weissleder, R. *Circulation* **2006**, *114* (14), 1504−1511.
(32) Bruckman, M. A.; Kaur, G.; Lee, L. A.; Xie, F.; Sepulveda, J.; Breitenkamp, R.; Zhang, X.; Joralemon, M.; Russell, T. P.; Emrick, T.; Wang, Q. *ChemBioChem* **2008**, *9* (4), 519−523.
(33) Caravan, P. *Chem. Soc. Rev.* **2006**, *35* (6), 512−523.
(34) Fitzgerald, K. T.; Holladay, C. A.; McCarthy, C.; Power, K. A.; Pandit, A.; Gallagher, W. M. *Small* **2011**, *7* (6), 705−717.
(35) Alsheikh-Ali, A. A.; Kitsios, G. D.; Balk, E. M.; Lau, J.; Ip, S. *Ann. Intern. Med.* **2010**, *153* (6), 387−395.
(36) Burtea, C.; Laurent, S.; Port, M.; Lancelot, E.; Ballet, S. b.; Rousseaux, O.; Toubeau, G. r.; Vander Elst, L.; Corot, C.; Muller, R. N. *J. Med. Chem.* **2009**, *52* (15), 4725−4742.
(37) Rouleau, L.; Berti, R.; Ng, V. W. K.; Matteau-Pelletier, C.; Lam, T.; Saboural, P.; Kakkar, A. K.; Lesage, F.; Rhéaume, E.; Tardif, J.-C. *Contrast Media Mol. Imaging* **2013**, *8* (1), 27−39.
(38) Peters, D.; Kastantin, M.; Kotamraju, V. R.; Karmali, P. P.; Gujraty, K.; Tirrell, M.; Ruoslahti, E. *Proc. Natl. Acad. Sci. U.S.A.* **2009**, *106* (24), 9815−9819.
(39) Makowski, M. R.; Forbes, S. C.; Blume, U.; Warley, A.; Jansen, C. H.; Schuster, A.; Wiethoff, A. J.; Botnar, R. M. *Atherosclerosis* **2012**, *222* (1), 43−49.
(40) Makowski, M. R.; Wiethoff, A. J.; Blume, U.; Cuello, F.; Warley, A.; Jansen, C. H.; Nagel, E.; Razavi, R.; Onthank, D. C.; Cesati, R. R.; Marber, M. S.; Schaeffter, T.; Smith, A.; Robinson, S. P.; Botnar, R. M. *Nat. Med.* **2011**, *17* (3), 383−388.
(41) Plummer, E. M.; Thomas, D.; Destito, G.; Shriver, L. P.; Manchester, M. *Nanomedicine* **2012**.
(42) Burtea, C.; Laurent, S.; Lancelot, E.; Ballet, S. b.; Murariu, O.; Rousseaux, O.; Port, M.; Vander Elst, L.; Corot, C.; Muller, R. N. *Mol. Pharmaceutics* **2009**, *6* (6), 1903−1919.
(43) Shriver, L. P.; Plummer, E. M.; Thomas, D. M.; Ho, S.; Manchester, M. *J. Mater. Chem. B* **2013**, *1* (39), 5256−5263.
(44) Uchida, M.; Kosuge, H.; Terashima, M.; Willits, D. A.; Liepold, L. O.; Young, M. J.; McConnell, M. V.; Douglas, T. *ACS Nano* **2011**, *5* (4), 2493−2502.
(45) Grobner, T. *Nephrol., Dial., Transplant.* **2005**, *21* (4), 1104−1108.
(46) Tweedle, M. F.; Wedeking, P.; Kumar, K. *Invest. Radiol.* **1995**, *30* (6), 372−380.
(47) Shellock, F. G.; Kanal, E. *J. Magn. Reson. Imaging* **1999**, *10* (3), 477−484.
(48) Prince, M. R.; Zhang, H.; Morris, M.; MacGregor, J. L.; Grossman, M. E.; Silberzweig, J.; DeLapaz, R. L.; Lee, H. J.; Magro, C. M.; Valeri, A. M. *Radiology* **2008**, *248* (3), 807−816.
(49) Wertman BA, R.; Altun, E.; Martin, D. R.; Mitchell, D. G.; Leyendecker, J. R.; O'Malley, R. B.; Parsons, D. J.; Fuller, E. R.; Semelka, R. C. *Radiology* **2008**, *248* (3), 799−806.
(50) Amirbekian, V.; Lipinski, M. J.; Briley-Saebo, K. C.; Amirbekian, S.; Aguinaldo, J. G.; Weinreb, D. B.; Vucic, E.; Frias, J. C.; Hyafil, F.; Mani, V.; Fisher, E. A.; Fayad, Z. A. *Proc. Natl. Acad. Sci. U.S.A.* **2007**, *104* (3), 961−966.
(51) van Tilborg, G. A.; Vucic, E.; Strijkers, G. J.; Cormode, D. P.; Mani, V.; Skajaa, T.; Reutelingsperger, C. P.; Fayad, Z. A.; Mulder, W. J.; Nicolay, K. *Bioconjugate Chem.* **2010**, *21* (10), 1794−1803.
(52) Wen, A. M.; Rambhia, P. H.; French, R. H.; Steinmetz, N. F. *J. Biol. Phys.* **2013**, *39* (2), 301−325.
(53) Rasmussen, L. M.; Hansen, P. R.; Nabipour, M. T.; Olesen, P.; Kristiansen, M. T.; Ledet, T. *Biochem. J.* **2001**, *360* (Pt 2), 363−370.
(54) Pueyo, M. E.; Gonzalez, W.; Nicoletti, A.; Savoie, F.; Arnal, J. F.; Michel, J. B. *Arterioscler. Thromb. Vasc. Biol.* **2000**, *20* (3), 645−651.
(55) Preiss, D. J.; Sattar, N. *Int J Clin Pract* **2007**, *61* (4), 697−701.